ACS OMEGA

http://pubs.acs.org/journal/acsodf
Article

Surface Engineering of Cu_2O Photocathodes via Facile Graphene Oxide Decoration for Improved Photoelectrochemical Water Splitting

Jiwon Heo, Hyojung Bae, Pratik Mane, Vishal Burungale, Chaewon Seong, and Jun-Seok Ha*

Cite This: *ACS Omega* 2023, 8, 32794−32803

ABSTRACT: Copper oxide (Cu_2O) has attracted significant interest as an efficient photocathode for photoelectrochemical (PEC) water splitting owing to its abundance, suitable band gap, and band-edge potential. Nevertheless, a high charge recombination rate restricts its practical photoconversion efficiency and reduces the PEC water-splitting performance. To address this challenge, we present the facile electrodeposition of graphene oxide (GO) on the Cu_2O photocathode surface. To determine the effect of varying GO weight percentages on PEC performance, varying amounts of GO were deposited on the Cu_2O photocathode surface. The optimally deposited GO−Cu_2O photocathode exhibited a photocurrent density of −0.39 to −1.20 mA/cm^2, which was three times that of a photocathode composed of pristine Cu_2O. The surface decoration of Cu_2O with GO reduced charge recombination and improved the PEC water-splitting performance. These composites can be utilized in strategies designed to address the challenges associated with low-efficiency Cu_2O photocathodes. The physicochemical properties of the prepared samples were comprehensively characterized by field-emission scanning electron microscopy, energy-dispersive spectroscopy, X-ray diffraction, Raman spectroscopy, UV−visible spectroscopy, and X-ray photoelectron spectroscopy. We believe that this research will pave the way for developing efficient Cu_2O-based photocathodes for PEC water splitting.

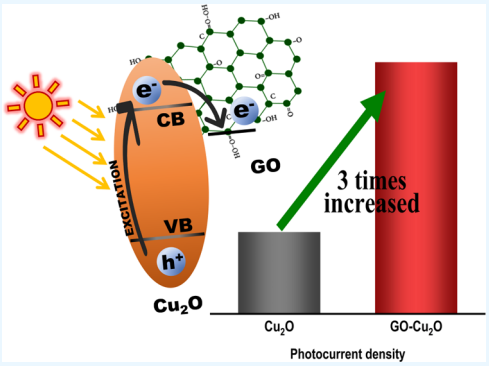

1. INTRODUCTION

Extensive use of fossil fuels releases significant amounts of carbon dioxide into the atmosphere, which aggravates global warming.[1] Therefore, there is an urgent need to develop alternative clean energy sources that could potentially replace fossil fuels. Hydrogen energy produced through photoelectrochemical (PEC) water splitting is the most promising method of producing energy from a sustainable clean energy production perspective.[2,3] The production of hydrogen via water splitting is an eco-friendly process, and the energy-mass density of hydrogen is greater than that of fossil fuels. PEC water splitting comprises two distinct half-cell reactions: hydrogen evolution reaction (HER) at the cathode and oxygen evolution reaction (OER) at the anode.[4,5] OER is a four-electron binding reaction, while HER is a two-electron transfer reaction

$$2H_2O \rightarrow O_2 + 4H^+ + 4e^- \quad (1)$$

$$4H^+ + 4e^- \rightarrow 2H_2 \quad (2)$$

PEC cells undergo HER and OER with their respective photoelectrodes in the electrolyte. Many photoelectrode materials, including TiO_2,[6−10] Cu_2O,[11−13] $BiVO_4$,[14−19] Fe_2O_3,[20−23] and C_3N_4,[24−26] have been investigated on the basis of these reactions. Among the p-type semiconductors that can be used as photoanodes, materials such as iron-based oxide,[27] ZnO, Cr_2O_3,[28] and Si with a band gap of 1.2 eV are available. Among them, we focused specifically on copper oxide (Cu_2O). P-type semiconducting Cu_2O is the promising photocathode candidate for PEC water splitting owing to its narrow direct band gap (2.1−2.3 eV),[29] high absorption coefficient, and high carrier mobility. Although the theoretical photocurrent density of Cu_2O is 14.7 mA/cm^2, the actual efficiency is low because of the recombination of photogenerated electron−hole pairs, which is a significant disadvantage.[29−31] In addition, charge carrier transport becomes difficult owing to the poor conductivity of Cu_2O. Therefore, additional research is required to develop rapidly transmitting and separating photogenerating carriers to reduce charge recombination. The method for enhancing the PEC performance of Cu_2O includes the formation of a heterojunction,

Received: June 1, 2023
Accepted: August 10, 2023
Published: August 28, 2023

https://doi.org/10.1021/acsomega.3c03585
ACS Omega 2023, 8, 32794−32803

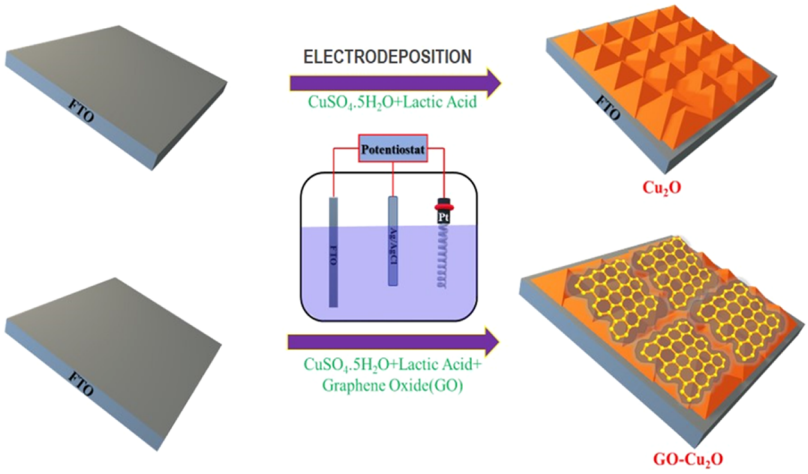

Figure 1. Schematic presentation of the fabrication process of a GO-decorated Cu_2O photocathode.

deposition of a cocatalyst, and surface modification. Wang et al. reported a ternary photocathode of Cu_2O sandwiched between NiS and Al nanoparticles.[11] This structure facilitates the transfer and separation of electron−hole pairs through light absorption, resulting in a high photocurrent density of −5.16 mA/cm^2 at 0 V, which is eight times higher than that of Cu_2O. The findings were attributed to the combining effect of Al with the surface plasmon resonance effect and the NiS loaded in the Cu_2O nanocube. Zhou et al. reported a photocathode that activated the surface with a Pt catalyst by employing FeOOH as a hole transfer layer to improve the minor form, which is a chronic shortcoming of Cu_2O.[29] They demonstrated that FeOOH improved the electrochemical stability of the Cu_2O photoelectrode by inhibiting the oxidation of Cu_2O and accelerating the hole extraction from within Cu_2O. Among the reported materials, graphene oxide (GO) has the potential to produce a high PEC yield when decorated on the Cu_2O surface. Because of its superior electrical conductivity and corrosion resistance, graphene and its derivatives are used to protect unstable semiconductors.[32−34] GO has been identified as a possible carbonaceous solid support or cocatalyst for boosting the photocatalytic activity of Cu_2O. The surface of GO is functionally equipped with epoxy and hydroxyl groups. Consequently, it has dual functionalities in three dimensions.[33,35,36]

This paper describes the cost-effective deposition of GO on the Cu_2O photocathode surface to overcome the low photoelectrochemical performance of Cu_2O. GO−Cu_2O composites were grown on fluorine-doped tin oxide (FTO) via electrochemical deposition. Modification of the surface of the Cu_2O photocathode enhanced both the light absorption and kinetics of PEC water splitting.

2. EXPERIMENTAL METHODS

2.1. Chemicals. Copper(II) sulfate pentahydrate ($CuSO_4 \cdot 5H_2O$, >99.0%, DUKSAN, Korea), sodium hydroxide (NaOH, >93.0%, DUKSAN, Korea), lactic acid ($C_3H_6O_3$, 85%, Sigma-Aldrich, Germany), and sodium sulfate (Na_2SO_4, >99%, Sigma-Aldrich, Germany) were used as received without further purification. In addition, fluorine-doped tin oxide (FTO)-coated glass (surface resistivity: 8 Ω/sq) and GO were purchased from Omniscience (Korea) and Standard Graphene (Korea), respectively.

2.2. Synthesis of GO−Cu_2O Photocathode. The electrodeposition method was used to fabricate a GO−Cu_2O composite on an FTO-coated glass substrate. First, FTO substrates were cleaned with a sonicator for 5 min in acetone, isopropyl alcohol, and deionized water sequentially. Next, we prepared a solution of 0.2 M $CuSO_4 \cdot 5H_2O$ and 3 M lactic acid. By using NaOH, the pH of the solution was adjusted to 12. Then, various weight percentages of GO were added to perform electrodeposition. Specifically, GO was added to the precursor solution and thoroughly mixed before the electrodeposition process. During the electrodeposition, the solution was kept at 60 °C and stirred slowly to ensure that GO was uniformly dispersed throughout the solution. The electrodeposition was performed at −0.6 V (vs Ag/AgCl) for 1 h using a three-electrode system. A Pt wire and Ag/AgCl (saturated KCl) were used as the counter and reference electrodes, respectively, with FTO serving as the working electrode. In addition, pristine Cu_2O was fabricated to compare the effects of GO on PEC properties. The stepwise fabrication process of the GO−Cu_2O photocathode is depicted in Figure 1.

2.3. Material Characterization. The effects of GO concentration on the morphological, structural, optical, and PEC properties of the GO−Cu_2O composite film were investigated using different techniques, including field-emission scanning electron microscopy (FE-SEM), energy-dispersive spectroscopy (EDS), Raman spectroscopy, X-ray diffraction (XRD), UV−visible (UV−vis) spectroscopy, X-ray optical spectroscopy (XPS), and potentiostatic techniques. The XRD studies were conducted at Chonnam National University's Energy Convergence Core Facility using an X'PERT PRO MRD PW3388/60 diffractometer, while the morphology, chemical composition, and optical properties of the products were characterized by FE-SEM (Hitachi, SU5000) and UV−vis spectroscopy (SHIMADZU, MPC-2200).

2.4. Photoelectrochemical Measurements. PEC properties were measured through electrochemical impedance spectroscopy (EIS), Mott−Schottky analysis, and linear sweep voltammetry (LSV) in a three-electrode system using a PARSTAT 4000 (AMETEK Princeton Applied Research) potentiostat. The surface area of the photoelectrode utilized for photoelectrochemical measurements was 1 cm^2. This was accomplished by restricting the length of the sample to 1 cm with insulating tape. The reference and counter electrodes

https://doi.org/10.1021/acsomega.3c03585
ACS Omega 2023, 8, 32794−32803

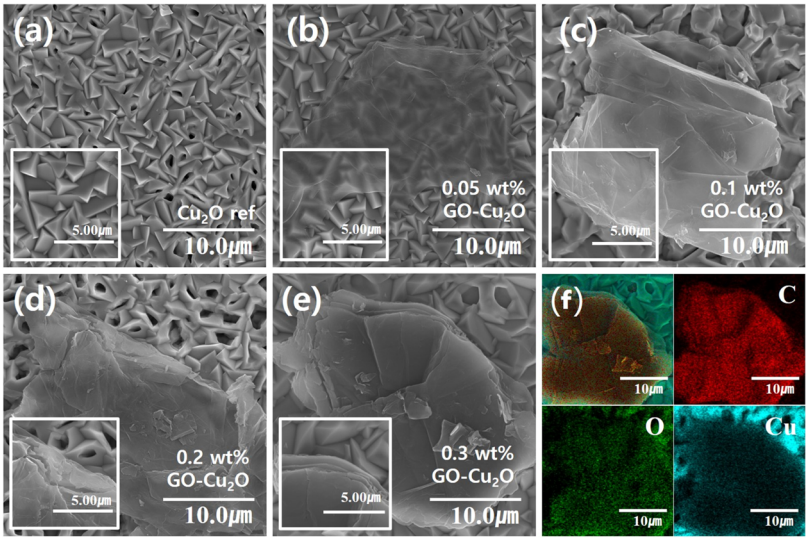

Figure 2. FE-SEM image of (a) Cu_2O reference, (b) 0.05 wt % GO−Cu_2O, (c) 0.1 wt % GO−Cu_2O, (d) 0.2 wt % GO−Cu_2O, and (e) 0.3 wt % GO−Cu_2O and (f) EDS of 0.3 wt % GO−Cu_2O composite. EDS images show the elemental mapping of C, O, and Cu.

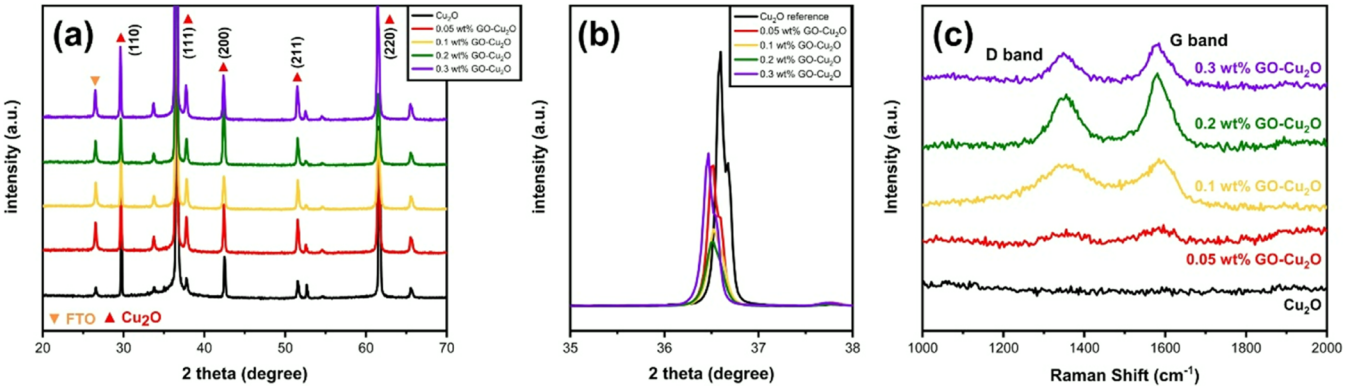

Figure 3. (a) XRD pattern, (b) comparison of the intensities of Cu (111) plane peaks, and (c) Raman spectra of Cu_2O and GO−Cu_2O.

were made of Ag/AgCl (saturated KCl) and Pt wire, respectively. Throughout all measurements, a 0.5 M Na_2SO_4 solution was used as the electrolyte. Simulated light (AM 1.5G, 100 mW/cm^2) was used for illumination. The potential value was converted into the reversible hydrogen electrode (RHE) scale using the Nernst equation, as given below[37]

$$E_{RHE} = E_{Ag/AgCl} + 0.059 \times pH + 0.1976 \quad (3)$$

3. RESULTS AND DISCUSSION

The schematic representation of the preparation process of the GO−Cu_2O composite is shown in Figure 1. The GO−Cu_2O composite was formed using a modified electrodeposition method. During the electrodeposition process, GO was added to the electrolyte solution containing Cu_2O precursor ions. The negatively charged GO sheets were attracted to the positively charged Cu_2O precursor ions and were incorporated into the growing Cu_2O film. Accordingly, a composite film comprising Cu_2O and GO was formed on the FTO substrate.

FE-SEM was used to examine the surface morphology of GO−Cu_2O composites synthesized by adding varying amounts of GO. Figure 2a depicts the formation of tetrahedral Cu_2O crystals on the FTO surface. The surface of GO−Cu_2O containing 0.05 wt % GO is depicted in Figure 2b. It displays a plate-shaped GO on the Cu_2O surface. It appears to be a single layer instead of multiple layers and is nearly transparent enough to penetrate the Cu_2O crystal structure. Figure 2c shows a surface image of GO−Cu_2O containing 0.1 wt % GO. Similarly, GO can be observed on Cu_2O crystals, and unlike the 0.05 wt % case, it can be observed that multiple layers are formed as opposed to a single thin layer. This phenomenon was also observed on the surface of GO−Cu_2O containing 0.2 and 0.3 wt % GO (Figure 2d,e). They appeared to produce more layers than either 0.05 or 0.1 wt % GO−Cu_2O. Figure 2f shows an EDS image of the composite material GO−Cu_2O, displaying the elemental mapping of C, O, and Cu. It validates the uniform deposition of GO on the surface of Cu_2O. The thickness of the electrodes was indeed measured using scanning electron microscopy (SEM) analysis. We found that the thickness of all of the electrodes, including the GO−Cu_2O composite and pristine Cu_2O, was approx. 4 μm.

The XRD patterns of Cu_2O and GO−Cu_2O composites are shown in Figure 3a. For Cu_2O, there were five distinct peaks corresponding to the (110), (111), (200), (211), and (220) directions, indicating the polycrystalline nature of Cu_2O. For GO−Cu_2O composites, no obvious peak of GO was observed in the XRD patterns because of its low content in the composites.[38] Figure 2b presents a comparison of the Cu_2O (111) peaks, and in the case of a sample containing GO, it can be seen that the intensity of the (111) peak decreases and is

https://doi.org/10.1021/acsomega.3c03585
ACS Omega 2023, 8, 32794−32803

shifted in a negative direction. In XRD, a shift to lower angles indicates that the crystal structure of Cu_2O has expanded or become more disordered. This may happen because GO sheets can enter between the layers of the Cu_2O crystal structure, increasing the distance between the crystal planes. The distance between the crystal planes of each sample is given in Table 1.

Table 1. Flat-Band Potential (E_{FB}), Slope of Mott−Schottky Plots, Acceptor Density (N_A), and Distance between the Crystal Planes (d) of Cu_2O and GO−Cu_2O Photocathodes

samples	E_{FB} [V_{RHE}]	slope	N_A [10^{18} cm^{-3}]	d [Å]
Cu_2O reference	0.77	-1.3274×10^{13}	1.35	2.45
0.05 wt % GO−Cu_2O	0.76	-1.1383×10^{13}	1.57	2.46
0.1 wt % GO−Cu_2O	0.66	-1.1377×10^{13}	1.57	2.46
0.2 wt % GO−Cu_2O	0.65	-1.0674×10^{13}	1.81	2.46
0.3 wt % GO−Cu_2O	0.69	-1.073×10^{13}	1.80	2.46

To confirm the existence of GO, Raman spectroscopy was further utilized. Carbon materials exhibit resonantly enhanced Raman scattering, making Raman spectroscopy a powerful tool for characterizing their molecular structures. The two main bands in the Raman spectrum are the D band at ∼1350 cm^{-1} and the G band at ∼1582 cm^{-1}, where the G and D bands are typical of carbon nanostructures.[39−41] Figure 3c presents the Raman spectra of Cu_2O and GO−Cu_2O composites. The G and D bands were obtained from all GO−Cu_2O samples except the pristine Cu_2O samples. As illustrated in Figure 3c, the intensity of the D and G bands was the lowest at 0.05 wt %, which increased with the GO content, reached a maximum of 0.2 wt %, and then began to decrease at 0.3 wt %. In the Raman spectrum of GO, the sum of the intensity of the D and G bands is proportional to the thickness of the GO layer.[42] Therefore, the thickness of the GO layer increased with the increase in GO content up to 0.2 wt %, but it decreased in the 0.3 wt % GO−Cu_2O sample.

X-ray photoelectron spectroscopy (XPS) was used to characterize the as-prepared GO−Cu_2O composite. To identify the presence of GO in the GO−Cu_2O composites, high-resolution C 1s XPS spectra were collected from the GO−Cu_2O composites. The fitted Cu 2p spectra of Cu_2O and GO−Cu_2O composites are shown in Figure 4a,b, respectively, revealing the oxidation state of Cu.[43] In the asymmetric core-level spectrum, the peaks correspond to the binding energies of Cu $2p_{3/2}$ at 932.0 eV and Cu $2p_{1/2}$ at 952.0 eV of Cu_2O.[43−45] Figure 4c shows the C 1s peak of GO−Cu_2O. It is deconvoluted into three peaks associated with graphitic sp^2 carbon (C═C/C−C) at 284.6 eV, carbonyl (C−O) at 286.0 eV, and carboxyl (O−C═O) functional groups at 288.2 eV.[43,46] Figure 4d presents a comparison of the C 1s peak intensities of the GO−Cu_2O photocathode. Furthermore, the thickness of the GO layer can be determined by comparing the intensity of the C 1s peak. As shown in Figure 4d, the peak intensity of the 0.2 wt % GO−Cu_2O sample was the highest, indicating that it had the most number of GO layers. The next

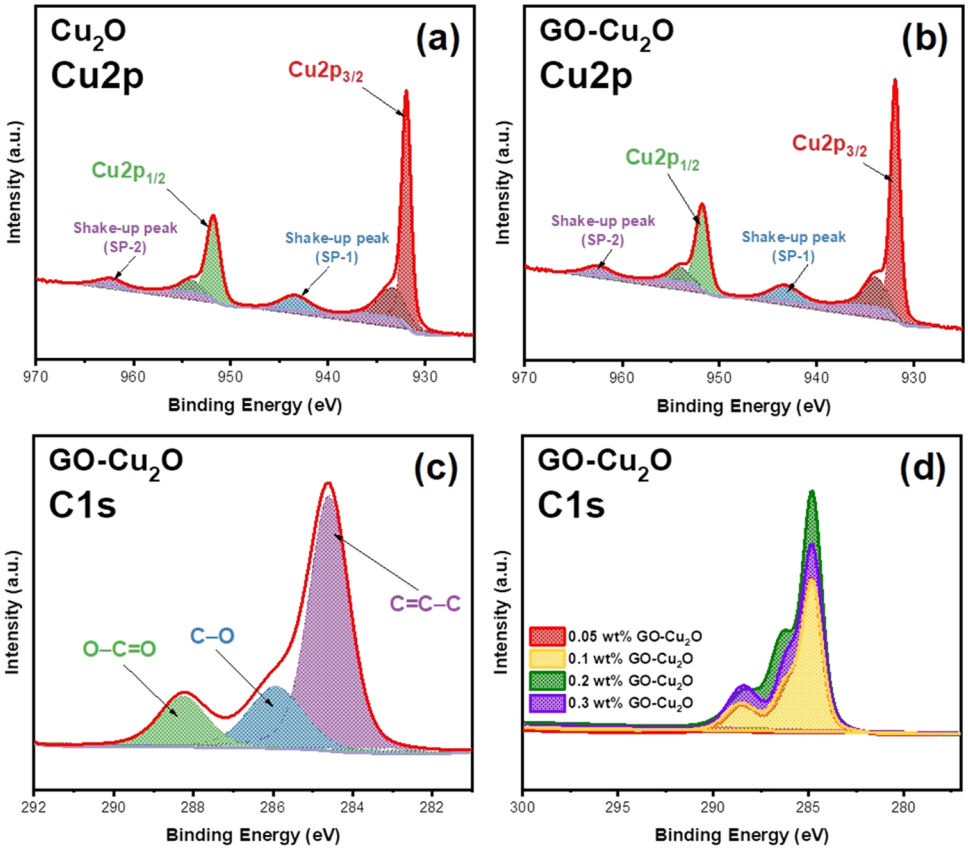

Figure 4. XPS spectra of (a) Cu 2p of Cu_2O, (b) Cu 2p of GO−Cu_2O, and (c) C 1s of GO−Cu_2O and (d) comparison of the C 1s peak intensities of GO−Cu_2O.

https://doi.org/10.1021/acsomega.3c03585
ACS Omega 2023, 8, 32794−32803

highest was the 0.3 wt % GO−Cu_2O sample, while there was little difference between the 0.05 and 0.1 wt % samples. This is consistent with the result that the intensity of the D and G bands in the Raman spectrum in Figure 3b was the strongest in the 0.2 wt % GO−Cu_2O sample.

The light-harvesting ability of synthesized GO−Cu_2O samples and their optical band gap energy were determined through diffuse reflectance spectroscopy (DRS) measurements. The reflectance spectra, as shown in Figure 5a, exhibited a significant decrease around 600 nm, indicating electron transitions occurring within the optical band gap. To accurately determine the precise value of the band gap, the reflectance values were converted to absorbance using Beer−Lambert's equation, eq 4.

$$\text{absorbance } A = \log \frac{100}{R} \tag{4}$$

where R is the reflectance.

And the DRS data were then transformed into the Kubelka−Munk function, $F(R)$, eq 5.

$$F(R) = \frac{\alpha}{S} = \frac{(1-R)^2}{2R} \tag{5}$$

where R is the reflectance, α is the absorbance coefficient, and S is the scattering coefficient. This conversion enabled a precise determination of the optical band gap energy, showcasing the light-harvesting potential of the GO−Cu_2O samples. By applying the Kubelka−Munk function, the direct band gap of GO−Cu_2O composites was estimated by plotting $(F(R)h\upsilon)^2$ against the photon energy ($h\upsilon$), yielding values of 2.11, 2.09, 2.08, 2.06, and 2.04 eV, respectively (inset of Figure 5b) and were comparable with the values reported in the literature.[47−49] Figure 5c illustrates the incident photon-to-current conversion efficiency (IPCE) of the Cu_2O and GO−Cu_2O composites, which were analyzed to determine their external and internal quantum efficiencies at 0 V vs RHE. This would enable the characterization of the photocurrent density in terms of wavelength. In general, the following equation describes the IPCE value

$$\text{IPCE} = \frac{1240 \times J}{\lambda \times P_{\text{light}}} \tag{6}$$

where J is the photocurrent density (mA/cm^2) and λ is the illumination wavelength. In the evaluated wavelength range, the IPCE of GO−Cu_2O was 7−18% greater than that of Cu_2O. The lowest IPCE was obtained for Cu_2O. Moreover, the IPCE improved when GO was added. The IPCE value reached its maximum of 28.9% in the GO−Cu_2O photocathode containing 0.2 wt % GO and then decreased in the GO−Cu_2O photocathode containing 0.3 wt % GO. According to the XPS measurement, the GO−Cu_2O photocathode containing 0.2 wt % C contained the highest weight percent of C. Thus, this result suggests that GO contributes to enhancing the quantum efficiency of Cu_2O.

The photocurrent response of each Cu_2O and GO−Cu_2O photocathode is depicted in Figure 6. Figure 6a−e shows the photochemical performance of Cu_2O and GO−Cu_2O samples measured using LSV. Each sample was analyzed 3 times; the average value of the photoelectric current density at 0 V (vs RHE) is shown in Figure 6f. The photoelectrochemical performance of the GO−Cu_2O samples was evaluated using LSV in a 0.5 M Na_2SO_4 aqueous solution under chopped 1 sun light illumination. As mentioned earlier, the surface area of the photoelectrode utilized for photoelectrochemical measurements was 1 cm^2. This was accomplished by restricting the

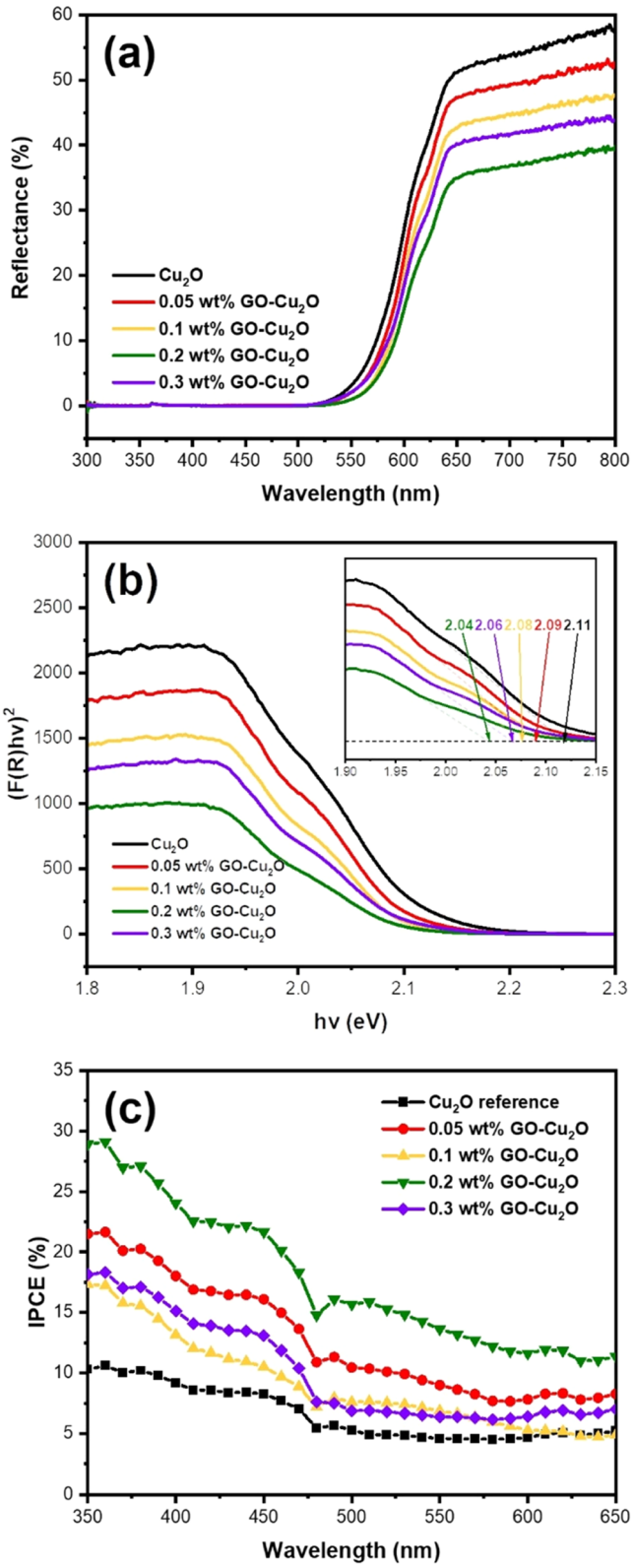

Figure 5. (a) Diffuse reflectance spectra, (b) Kubelka−Munk plots for the band gap energy calculation, and (c) efficiency of incident photon-to-current conversion (IPCE) of the Cu_2O and GO−Cu_2O composites.

https://doi.org/10.1021/acsomega.3c03585
ACS Omega 2023, 8, 32794−32803

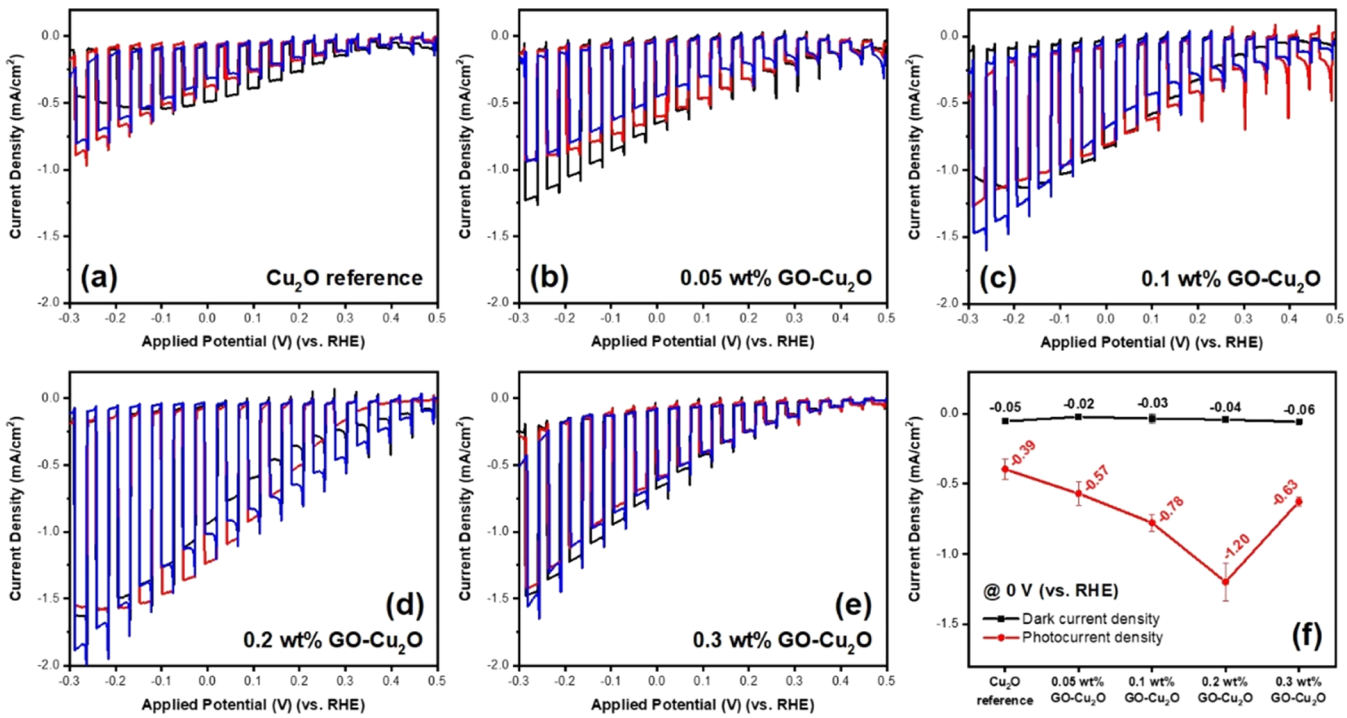

Figure 6. LSV plots of (a) Cu_2O, (b) 0.05 wt % GO−Cu_2O, (c) 0.1 wt % GO−Cu_2O, (d) 0.2 wt % GO−Cu_2O, and (e) 0.3 wt % GO−Cu_2O photocathodes and (f) comparison of the average values of photocurrent density at 0 V (vs RHE).

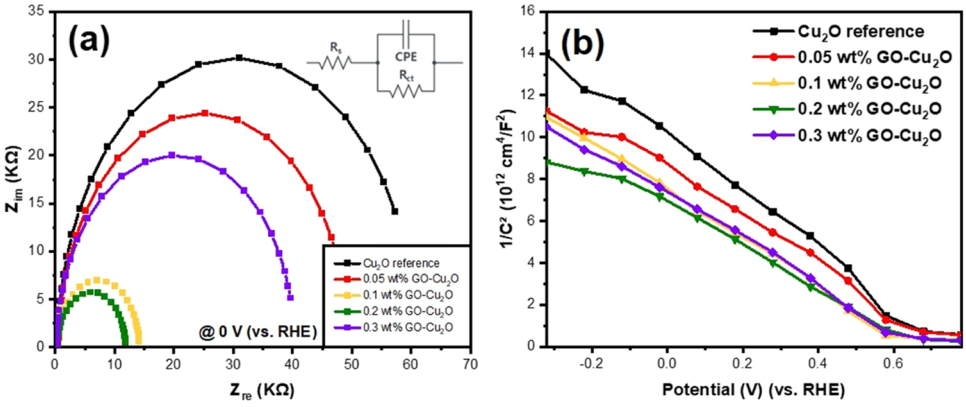

Figure 7. (a) EIS spectra and (b) Mott−Schottky plots of Cu_2O and GO−Cu_2O.

length of the sample to 1 cm with insulating tape. The LSV of GO-modified samples was compared with that of an unmodified Cu_2O electrode, and the photocurrent density was found to increase up to three times after GO addition compared to Cu_2O alone. The increase in photocurrent density varied with the weight percentage of added GO: at 0.05 wt %, the photocurrent density increased by a factor of 1.5; at 0.1 wt %, it increased by a factor of 2.0; at 0.2 wt %, it increased by a factor of 3.1; and at 0.3 wt %, it increased by a factor of 1.6. Among the GO−Cu_2O samples, the sample prepared by adding 0.2 wt % of Cu_2O demonstrated the highest PEC performance, as shown in Figure 6f, which displays the photocurrent and dark current densities at the same voltage of 0 V (vs RHE). The dark current density for each sample ranged from −0.02 to −0.06 mA/cm^2, with no significant differences. By contrast, the photocurrent density for the Cu_2O reference was the lowest at −0.39 mA/cm^2 and gradually increased to −0.57 and −0.78 mA/cm^2 as the amount of GO was increased, with the highest photocurrent density measured at −1.20 mA/cm^2 for 0.2 wt % GO. However, the photocurrent density for the 0.3 wt % GO−Cu_2O sample decreased to −0.63 mA/cm^2.

The charge transfer capability between Cu_2O and GO−Cu_2O photoelectrodes was compared using electrochemical impedance spectroscopy (EIS) analysis. The Nyquist plots in Figure 7a depict the results. The inset of Figure 7a presents the corresponding electrical equivalent circuit, which includes the solution resistance (R_s), a constant phase element representing double-layer capacitance (C_{PE}), and the charge transfer resistance (R_{ct}) connected in parallel with C_{PE}. The rate of charge transfer is reflected by the radius of the arc on the Nyquist plot as reported.[32,50,51] The semicircle diameter of pristine Cu_2O is the largest, while the diameter of the GO−Cu_2O photocathode containing 0.05 wt % GO is smaller than that of pristine Cu_2O. With increasing amounts of GO, the diameter of the semicircle decreases, reaching a minimum value for 0.2 wt % GO−Cu_2O, and then increases again for 0.3 wt % GO−Cu_2O. The diameter of the semicircle is an

https://doi.org/10.1021/acsomega.3c03585
ACS Omega 2023, 8, 32794−32803

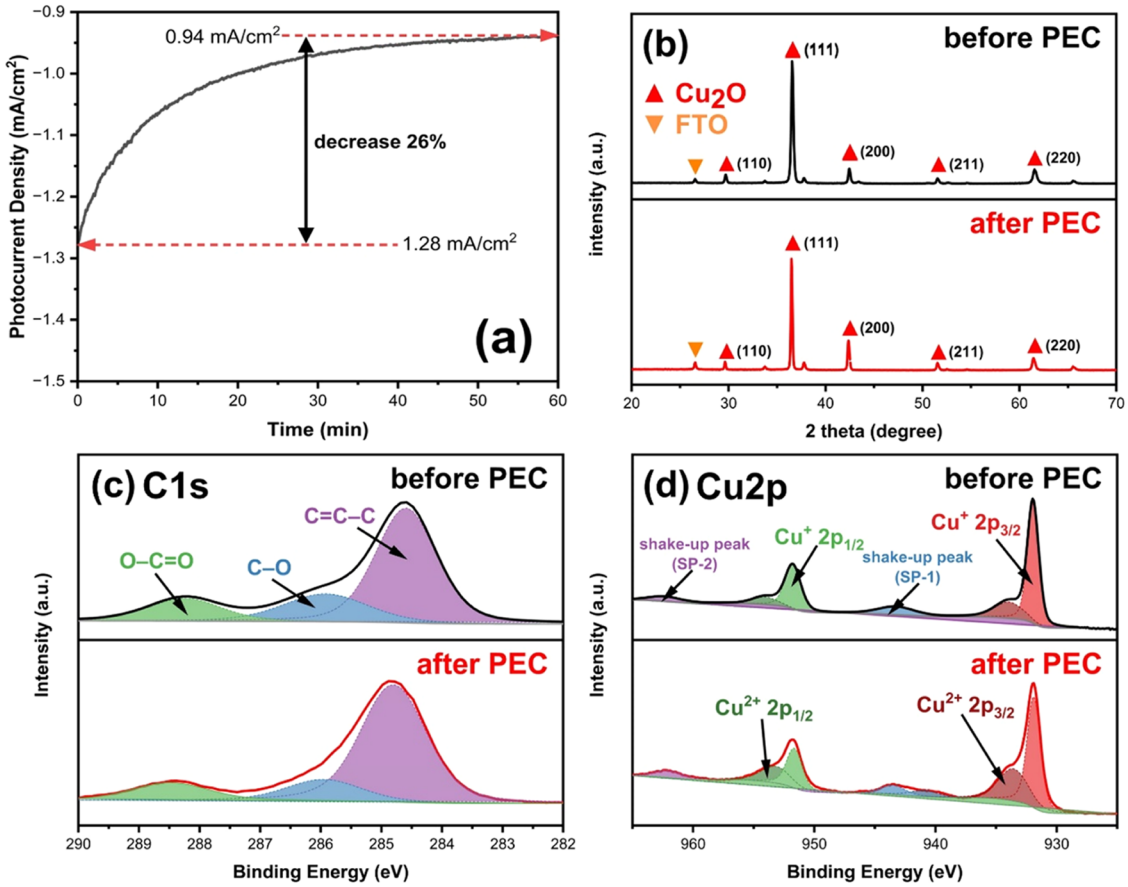

Figure 8. (a) Electrochemical stability test, (b) XRD pattern and XPS spectra for (c) C 1s and (d) Cu 2p of the 0.2 wt % GO−Cu_2O photocathode before and after PEC.

indicator of charge transfer resistance (R_{ct}) at high frequencies, Thus, R_{ct} decreased with increasing amounts of GO, reaching a minimum value for GO−Cu_2O containing 0.2 wt % GO. However, when the amount of GO was increased beyond 0.2 wt %, R_{ct} increased again. This trend is consistent with the analysis results described above, and it indicates that the charge transfer process of GO−Cu_2O is faster than that of Cu_2O. These findings provide insights into the impact of GO on the charge transfer properties of the photocathodes.

Mott−Schottky analysis was used to determine the donor density and flat-band potential (E_{FB}) at the semiconductor−liquid interface, as depicted in Figure 7b. In Figure 7b, all Cu_2O and GO−Cu_2O photocathodes exhibit a negative slope, indicating that they are p-type semiconductors.[52] The calculated E_{FB} values for each photoanode range from pristine Cu_2O to 0.3 wt % GO−Cu_2O, followed by 0.77, 0.76, 0.66, 0.65, and 0.69 V (vs RHE), respectively. In addition, the donor density is inversely proportional to the Mott−Schottky slope.[43,53] This demonstrates that the donor density is lowest in pure Cu_2O, gradually increases with increasing amounts of GO, and then decreases after reaching a maximum of 0.2 wt % of GO. E_{FB} and donor density correspond to other analysis results, such as photocurrent density. This can be attributed to the fact that even though the amount of GO added during the GO−Cu_2O electrodeposition increased, the amount of GO on the surface of the electrode decreased. The Cu_2O sample had the lowest acceptor density, while the GO-modified Cu_2O had a higher acceptor density than pristine Cu_2O. The 0.2 wt % GO−Cu_2O sample had the highest acceptor density, followed by 0.3 wt % GO−Cu_2O. When there are more defects or impurities in a material, the acceptor density can increase. Thus, the addition of GO can introduce defects or impurities into the Cu_2O film, leading to an increase in the acceptor density. This is also supported by the lower angle shift of the Cu_2O (111) peak in Figure 3b. Alternatively, it could be due to changes in the lattice parameters, resulting from the incorporation of GO. The flat-band potential (E_{FB}), Mott−Schottky slope values, acceptor densities (N_A), and distance between the crystal planes (d) of Cu_2O and GO−Cu_2O photocathodes are summarized in Table 1.

Figure 8a shows the electrochemical stability test of the GO−Cu_2O sample. The change in photocurrent density under the RHE 0V voltage was measured. Measurements for 30 min showed that the photocurrent density decreased by about 26% from −1.28 to −0.94 mA/cm^2. Following the PEC reaction, XRD (Figure 8b) and XPS (Figure 8c,d) analyses were performed to further characterize the GO−Cu_2O photocathodes. The XRD pattern of the GO−Cu_2O phase showed no significant change, with only a slight increase in the intensity of the (200) plane. This suggests that the GO−Cu_2O crystal phase was stable even after the PEC experiment. Moreover, the C 1s XPS spectra showed that GO remained in Cu_2O after the PEC reaction (Figure 8c). In Figure 8d, the Cu^{2+} species dominate the spectra prior to the PEC, with two satellite peaks for Cu $2p_{1/2}$ and Cu $2p_{3/2}$. After PEC, the intensity of the peaks for Cu^+ $2p_{1/2}$ and Cu^+ $2p_{3/2}$ increased compared to before PEC; however, there was no significant change in the overall spectrum. These observations indicate

https://doi.org/10.1021/acsomega.3c03585
ACS Omega 2023, 8, 32794−32803

the stability of the GO−Cu_2O composite toward PEC reactions.

On the basis of the above characterization and experimental results, a reasonable mechanism of the GO−Cu_2O photocathode for the charge transfer process is proposed, as shown in Figure 9. The photocurrent density increases when GO is added to Cu_2O because of the improved charge transport and light absorption properties of the resulting GO−Cu_2O composite film. In the GO−Cu_2O composite film, the incorporation of GO sheets enhances the electron transport properties of the Cu_2O film by providing additional pathways for electron transport. It reduces the charge recombination and enhances the charge transport across the film. Additionally, the GO sheets have a high surface area, which increases the number of active sites available for the PEC reaction and enhances the reaction kinetics. Moreover, the incorporation of GO into the Cu_2O film also affects the band gap of the resulting composite. The GO sheets have a higher work function compared to Cu_2O, which creates an energy level alignment between the two materials. This alignment results in a reduction of the band gap of the composite film, which enhances the light absorption properties of the film in the visible region of the electromagnetic spectrum. Overall, the incorporation of GO into the Cu_2O film results in an enhancement of both the charge transport and light absorption properties of the composite film. This improvement leads to an increase in the photoelectric current density of the GO−Cu_2O composite film compared to the pristine Cu_2O film.

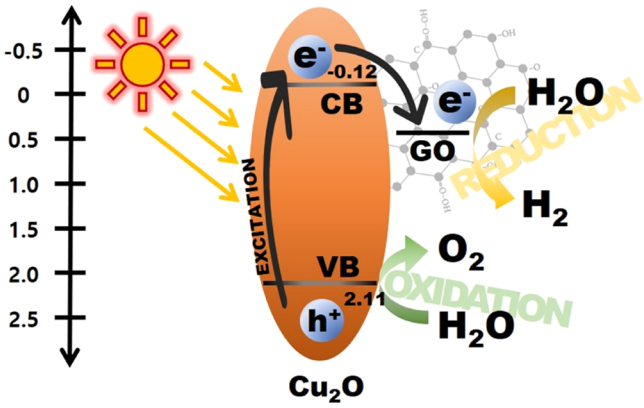

Figure 9. Schematic illustration of the charge transfer mechanism in the GO−Cu_2O photocathode.

In addition, for comparison purposes, we have summarized photocurrent density data from other significant references in Table 2. In comparison to other Cu_2O-based photoelectrodes, our study focused on forming a composite with Cu_2O using graphene oxide (GO). While our composite did not achieve the highest level of performance, it demonstrated notable compliance with respect to photocurrent density. Additionally, one significant advantage of our approach was the simplicity of the manufacturing process, which involved a single-step method. This simplicity stands in contrast to the more complex fabrication methods employed in other Cu_2O-based photoelectrodes. By offering a balance between performance and ease of fabrication, our GO−Cu_2O composite presents a promising and practical option for efficient photoelectrochemical water-splitting applications.

Table 2. Comparison of Photocurrent Densities in Cu_2O-Based Photocathodes for PEC Water Splitting

	measuring conditions			
photoelectrode	electrolyte	potential	photocurrent density [mA/cm^2]	refs
GO−Cu_2O	0.5 M Na_2SO_4	0 V (vs RHE)	−1.20	this work
Cu/Al/Cu_2O	0.1 M Na_2SO_4	0 V (vs RHE)	−2.16	11
FeOOH/Cu_2O	0.1 M Na_2SO_4	0 V (vs RHE)	−1.5	54
Ni-doped Cu_2O	0.3 M Na_2SO_3	0 V (vs RHE)	−0.83	31
Cu_2O thin film	0.1 M Na_2SO_4	0.2 V (vs Ag/Ag-Cl)	−0.95	55
Cu_2O thin film	1 M Na_2SO_4	−0.1 V (vs RHE)	−1.0	56
Cu_2O/Ni-CuBTC	0.5 M Na_2SO_4 buffered with 0.2 M PBS	0 V (vs RHE)	−1.51	57
Cu_2O/CuO	pH 6.5 aqueous solution	0 V (vs RHE)	−1.21	58
Cu_2O/CuO/Cu_2O	0.5 M Na_2SO_4	0 V (vs RHE)	−2.3	59
CuO/Cu_2O nanoflake/nanowire heterostructure	0.5 M Na_2SO_4	−0.3 V (vs Ag/Ag-Cl)	−1.9	60
Pt/n-Cu_2O/p-Cu_2O	0.5 M Na_2SO_4	0 V (vs RHE)	−2.0	61
Cu_2O/ZnO/TiN	0.5 M Na_2SO_4	0 V (vs RHE)	−1.4	62

4. CONCLUSIONS

In this study, the addition of GO to Cu_2O demonstrated improved photoelectrochemical performance. The GO−Cu_2O composite was successfully electrodeposited on the FTO substrate, and the optimal GO addition amount was determined through LSV photocurrent density measurements. Characterization techniques, including XRD, Raman, and XPS, confirmed the formation of the GO−Cu_2O composite. The analysis revealed that even with increased GO addition, the generated amount of GO on the electrode surface remained below 0.2 wt % for a total addition of 0.3 wt %, as supported by XPS analysis. The GO−Cu_2O photocathode exhibited a photocurrent density of −1.20 mA/cm^2 at 0 V (vs RHE) for the 0.2 wt % GO composition, which was 3 times higher than that of Cu_2O (−0.4 mA/cm^2). The incorporation of GO led to enhanced light absorption and quantum efficiency, as evidenced by IPCE measurements. Furthermore, the EIS results demonstrated that GO−Cu_2O exhibited a lower charge transfer resistance compared to Cu_2O. Overall, the experimental findings indicate that GO contributes to the improvement of the PEC characteristics of Cu_2O, making it a promising catalyst for enhancing its performance. However, it is important to note that excessive deposition of GO can potentially result in adverse effects. Moreover, further investigation is required to address the issue of low stability. And additional research is needed to understand the specific factors influencing the Raman spectra and the intensity of the D and G bands in the GO−Cu_2O composite.

■ AUTHOR INFORMATION

Corresponding Author

Jun-Seok Ha − *Department of Chemicals Engineering, Chonnam National University, Gwangju 61186, Korea;*

https://doi.org/10.1021/acsomega.3c03585
ACS Omega 2023, 8, 32794−32803

Optoelectronics Convergence Research Center, Chonnam National University, Gwangju 61186, Korea; orcid.org/0000-0003-3216-3093; Email: jsha@jnu.ac.kr

Authors

Jiwon Heo − *Department of Chemicals Engineering, Chonnam National University, Gwangju 61186, Korea*

Hyojung Bae − *Optoelectronics Convergence Research Center, Chonnam National University, Gwangju 61186, Korea*

Pratik Mane − *Department of Chemicals Engineering, Chonnam National University, Gwangju 61186, Korea*

Vishal Burungale − *Department of Chemicals Engineering, Chonnam National University, Gwangju 61186, Korea*

Chaewon Seong − *Department of Chemicals Engineering, Chonnam National University, Gwangju 61186, Korea*

Complete contact information is available at: https://pubs.acs.org/10.1021/acsomega.3c03585

Notes

The authors declare no competing financial interest.

■ ACKNOWLEDGMENTS

This research was supported by the National Research Foundation of Korea (NRF) funded by the Ministry of Education, Science, and Technology (2018R1A6A1A03024334) and the Basic Science Research Capacity Enhancement Project through the Korea Basic Science Institute (National Research Facilities and Equipment Center) grant funded by the Ministry of Education (Grant No. 2019R1A6C1010024).

■ REFERENCES

(1) Nejat, P.; Jomehzadeh, F.; Taheri, M. M.; Gohari, M.; Muhd, M. Z. A Global Review of Energy Consumption, CO2 Emissions and Policy in the Residential Sector (with an Overview of the Top Ten CO2 Emitting Countries). *Renewable Sustainable Energy Rev.* **2015**, *43*, 843−862.

(2) Minggu, L. J.; Wan Daud, W. R.; Kassim, M. B. An Overview of Photocells and Photoreactors for Photoelectrochemical Water Splitting. *Int. J. Hydrogen Energy* **2010**, *35*, 5233−5244.

(3) Joy, J.; Mathew, J.; George, S. C. Nanomaterials for Photoelectrochemical Water Splitting − Review. *Int. J. Hydrogen Energy* **2018**, *43*, 4804−4817.

(4) Shao, M.; Chang, Q.; Dodelet, J. P.; Chenitz, R. Recent Advances in Electrocatalysts for Oxygen Reduction Reaction. *Chem. Rev.* **2016**, *116*, 3594−3657.

(5) Zhang, Y.; Dou, G.; Sun, Z.; Guo, M.; Li, Y. Establishment of Physical and Mathematical Models for Sr0.95Ba0.05TiO3 Memristor. *Int. J. Bifurcation Chaos* **2017**, *27*, No. 1750148.

(6) Yu, Z.; Liu, H.; Zhu, M.; Li, Y.; Li, W. Interfacial Charge Transport in 1D TiO2 Based Photoelectrodes for Photoelectrochemical Water Splitting. *Small* **2021**, *17*, No. 1903378.

(7) Zu, M.; Zhou, X.; Zhang, S.; Qian, S.; Li, D. S.; Liu, X.; Zhang, S. Sustainable Engineering of TiO2-Based Advanced Oxidation Technologies: From Photocatalyst to Application Devices. *J. Mater. Sci. Technol.* **2021**, *78*, 202−222.

(8) Celebi, N.; Aydin, M. Y.; Soysal, F.; Ciftci, Y. O.; Salimi, K. Ligand-Free Fabrication of Au/TiO2 Nanostructures for Plasmonic Hot-Electron-Driven Photocatalysis: Photoelectrochemical Water Splitting and Organic-Dye Degredation. *J. Alloys Compd.* **2021**, *860*, No. 157908.

(9) Ansón-Casaos, A.; Hernández-Ferrer, J.; Vallan, L.; Xie, H.; Lira-Cantú, M.; Benito, A. M.; Maser, W. K. Functionalized Carbon Dots on TiO2 for Perovskite Photovoltaics and Stable Photoanodes for Water Splitting. *Int. J. Hydrogen Energy* **2021**, *46*, 12180−12191.

(10) Liu, Y.; Wang, M.; Zhang, B.; Yan, D.; Xiang, X. Mediating the Oxidizing Capability of Surface-Bound Hydroxyl Radicals Produced by Photoelectrochemical Water Oxidation to Convert Glycerol into Dihydroxyacetone. *ACS Catal.* **2022**, *12*, 6946−6957.

(11) Wang, P.; Liu, Z.; Han, C.; Zou, Y.; Tong, Z.; Tan, B. Decorating Cu2O Photocathode with Cu/Al Bimetallic Layer for Enhanced Photoelectrochemical Water Splitting. *Int. J. Energy Res.* **2022**, *46*, 16991−17002.

(12) Pan, L.; Liu, Y.; Yao, L.; Ren, D.; Sivula, K.; Grätzel, M.; Hagfeldt, A. Cu2O Photocathodes with Band-Tail States Assisted Hole Transport for Standalone Solar Water Splitting. *Nat. Commun.* **2020**, *11*, No. 318.

(13) Zhu, J.; Jiang, E.; Wang, X.; Pan, Z.; Xu, X.; Ma, S.; Kang Shen, P.; Pan, L.; Eguchi, M.; Nanjundan, A. K.; Shapter, J.; Yamauchi, Y. Gram-Scale Production of Cu3P-Cu2O Janus Nanoparticles into Nitrogen and Phosphorous Doped Porous Carbon Framework as Bifunctional Electrocatalysts for Overall Water Splitting. *Chem. Eng. J.* **2022**, *427*, No. 130946.

(14) Jin, S.; Ma, X.; Pan, J.; Zhu, C.; Saji, S. E.; Hu, J.; Xu, X.; Sun, L.; Yin, Z. Oxygen Vacancies Activating Surface Reactivity to Favor Charge Separation and Transfer in Nanoporous BiVO4 Photoanodes. *Appl. Catal., B* **2021**, *281*, No. 119477.

(15) Liang, X.; Wang, P.; Tong, F.; Liu, X.; Wang, C.; Wang, M.; Zhang, Q.; Wang, Z.; Liu, Y.; Zheng, Z.; Dai, Y.; Huang, B. Bias-Free Solar Water Splitting by Tetragonal Zircon BiVO4 Nanocrystal Photocathode and Monoclinic Scheelite BiVO4 Nanoporous Photoanode. *Adv. Funct. Mater.* **2021**, *31*, No. 2008656.

(16) Tang, Y.; Wang, R.; Yang, Y.; Yan, D.; Xiang, X. Highly Enhanced Photoelectrochemical Water Oxidation Efficiency Based on Triadic Quantum Dot/Layered Double Hydroxide/BiVO4 Photoanodes. *ACS Appl. Mater. Interfaces* **2016**, *8*, 19446−19455.

(17) Bai, S.; Chu, H.; Xiang, X.; Luo, R.; He, J.; Chen, A. Fabricating of Fe2O3/BiVO4 Heterojunction Based Photoanode Modified with NiFe-LDH Nanosheets for Efficient Solar Water Splitting. *Chem. Eng. J.* **2018**, *350*, 148−156.

(18) Zhang, J.; Wei, X.; Zhao, J.; Zhang, Y.; Wang, L.; Huang, J.; She, H.; Wang, Q. Electronegative Cl− Modified BiVO4 Photoanode Synergized with Nickel Hydroxide Cocatalyst for High-Performance Photoelectrochemical Water Splitting. *Chem. Eng. J.* **2023**, *454*, No. 140081.

(19) Wang, L.; Liu, Z.; Zhang, J.; Jia, Y.; Huang, J.; Mei, Q.; Wang, Q. Boosting Charge Separation of BiVO4 Photoanode Modified with 2D Metal-Organic Frameworks Nanosheets for High-Performance Photoelectrochemical Water Splitting. *Chin. Chem. Lett.* **2022**, *34*, No. 108007.

(20) Kyesmen, P. I.; Nombona, N.; Diale, M. Heterojunction of Nanostructured α-Fe2O3/CuO for Enhancement of Photoelectrochemical Water Splitting. *J. Alloys Compd.* **2021**, *863*, No. 158724.

(21) Quang, N. D.; Hu, W.; Chang, H. S.; Van, P. C.; Viet, D. D.; Jeong, J. R.; Seo, D. B.; Kim, E. T.; Kim, C.; Kim, D. Fe2O3 Hierarchical Tubular Structure Decorated with Cobalt Phosphide (CoP) Nanoparticles for Efficient Photoelectrochemical Water Splitting. *Chem. Eng. J.* **2021**, *417*, No. 129278.

(22) Lei, B.; Xu, D.; Wei, B.; Xie, T.; Xiao, C.; Jin, W.; Xu, L. In Situ Synthesis of α-Fe2o3/Fe3o4heterojunction Photoanode via Fast Flame Annealing for Enhanced Charge Separation and Water Oxidation. *ACS Appl. Mater. Interfaces* **2021**, *13*, 4785−4795.

(23) Huang, X.; Yang, L.; Hao, S.; Zheng, B.; Yan, L.; Qu, F.; Asiri, A. M.; Sun, X. N-Doped Carbon Dots: A Metal-Free Co-Catalyst on Hematite Nanorod Arrays toward Efficient Photoelectrochemical Water Oxidation. *Inorg. Chem. Front.* **2017**, *4*, 537−540.

(24) Velusamy, P.; Sathiya, M.; Liu, Y.; Liu, S.; Babu, R. R.; Aly Saad Aly, M.; Elangovan, E.; Chang, H.; Mao, L.; Xing, R. Investigating the Effect of Nd3+ Dopant and the Formation of G-C3N4/BiOI Heterostructure on the Microstructural, Optical and Photoelectrocatalytic Properties of g-C3N4. *Appl. Surf. Sci.* **2021**, *561*, No. 150082.

(25) Nekouei, F.; Nekouei, S.; Pouzesh, M.; Liu, Y. Porous-CdS/Cu2O/Graphitic-C3N4 Dual p-n Junctions as Highly Efficient

Photo/Catalysts for Degrading Ciprofloxacin and Generating Hydrogen Using Solar Energy. *Chem. Eng. J.* **2020**, *385*, No. 123710.
(26) Gao, Z.; Chen, K.; Wang, L.; Bai, B.; Liu, H.; Wang, Q. Aminated Flower-like ZnIn2S4 Coupled with Benzoic Acid Modified g-C3N4 Nanosheets via Covalent Bonds for Ameliorated Photocatalytic Hydrogen Generation. *Appl. Catal., B* **2020**, *268*, No. 118462.
(27) Jang, Y. J.; Lee, J. S. Photoelectrochemical Water Splitting with P-Type Metal Oxide Semiconductor Photocathodes. *ChemSusChem* **2019**, *12*, 1835−1845.
(28) Sekizawa, K.; Oh-Ishi, K.; Morikawa, T. Photoelectrochemical Water-Splitting over a Surface Modified p-Type Cr2O3 Photocathode. *Dalton Trans.* **2020**, *49*, 659−666.
(29) Zhou, M.; Guo, Z.; Liu, Z. FeOOH as Hole Transfer Layer to Retard the Photocorrosion of Cu2O for Enhanced Photoelectrochemical Performance. *Appl. Catal., B* **2020**, *260*, No. 118213.
(30) Paracchino, A.; Laporte, V.; Sivula, K.; Grätzel, M.; Thimsen, E. Highly Active Oxide Photocathode for Photoelectrochemical Water Reduction. *Nat. Mater.* **2011**, *10*, 456−461.
(31) Zhang, M.; Wang, J.; Xue, H.; Zhang, J.; Peng, S.; Han, X.; Deng, Y.; Hu, W. Acceptor-Doping Accelerated Charge Separation in Cu2O Photocathode for Photoelectrochemical Water Splitting: Theoretical and Experimental Studies. *Angew. Chem., Int. Ed.* **2020**, *59*, 18463−18467.
(32) Zhong, X.; Song, Y.; Cui, A.; Mu, X.; Li, L.; Han, L.; Shan, G.; Liu, H. Adenine-Functionalized Graphene Oxide as a Charge Transfer Layer to Enhance Activity and Stability of Cu2O Photocathode for CO2 Reduction Reaction. *Appl. Surf. Sci.* **2022**, *591*, No. 153197.
(33) Huang, X.; Zeng, Z.; Fan, Z.; Liu, J.; Zhang, H. Graphene-Based Electrodes. *Adv. Mater.* **2012**, *24*, 5979−6004.
(34) Yin, Z.; Zhu, J.; He, Q.; Cao, X.; Tan, C.; Chen, H.; Yan, Q.; Zhang, H. Graphene-Based Materials for Solar Cell Applications. *Adv. Energy Mater.* **2014**, *4*, No. 1300574.
(35) Loh, K. P.; Bao, Q.; Eda, G.; Chhowalla, M. Graphene Oxide as a Chemically Tunable Platform for Optical Applications. *Nat. Chem.* **2010**, *2*, 1015−1024.
(36) Jahan, M.; Liu, Z.; Loh, K. P. A Graphene Oxide and Copper-Centered Metal Organic Framework Composite as a Tri-Functional Catalyst for HER, OER, and ORR. *Adv. Funct. Mater.* **2013**, *23*, 5363−5372.
(37) Burungale, V.; Bae, H.; Mane, P.; Rho, H.; Ryu, S. W.; Kang, S. H.; Ha, J. S. Improved Performance of CNT-Pd Modified Cu2O Supported on Nickel Foam for Hydrogen Evolution Reaction in Basic Media. *J. Mol. Liq.* **2021**, *343*, No. 117612.
(38) Lee, J. S.; You, K. H.; Park, C. B. Highly Photoactive, Low Bandgap TiO 2 Nanoparticles Wrapped by Graphene. *Adv. Mater.* **2012**, *24*, 1084−1088.
(39) Jorio, A.; Souza Filho, A. G. Raman Studies of Carbon Nanostructures. *Annu. Rev. Mater. Res.* **2016**, *46*, 357−382.
(40) Kudin, K. N.; Ozbas, B.; Schniepp, H. C.; Prud'homme, R. K.; Aksay, I. A.; Car, R. Raman Spectra of Graphite Oxide and Functionalized Graphene Sheets. *Nano Lett.* **2008**, *8*, 36−41.
(41) Claramunt, S.; Varea, A.; López-Díaz, D.; Velázquez, M. M.; Cornet, A.; Cirera, A. The Importance of Interbands on the Interpretation of the Raman Spectrum of Graphene Oxide. *J. Phys. Chem. C* **2015**, *119*, 10123−10129.
(42) Kostiuk, D.; Bodik, M.; Siffalovic, P.; Jergel, M.; Halahovets, Y.; Hodas, M.; Pelletta, M.; Pelach, M.; Hulman, M.; Spitalsky, Z.; Omastova, M.; Majkova, E. Reliable Determination of the Few-Layer Graphene Oxide Thickness Using Raman Spectroscopy. *J. Raman Spectrosc.* **2016**, *47*, 391−394.
(43) An, X.; Li, K.; Tang, J. Cu2O/Reduced Graphene Oxide Composites for the Photocatalytic Conversion of CO2. *ChemSusChem* **2014**, *7*, 1086−1093.
(44) Torrisi, L.; Silipigni, L.; Cutroneo, M.; Torrisi, A. Graphene Oxide as a Radiation Sensitive Material for XPS Dosimetry. *Vacuum* **2020**, *173*, No. 109175.
(45) Vasquez, R. P. Cu2O by XPS. *Surf. Sci. Spectra* **1998**, *5*, 257−261.
(46) Zhang, Z.; Sun, L.; Wu, Z.; Liu, Y.; Li, S. Facile Hydrothermal Synthesis of CuO-Cu2O/GO Nanocomposites for the Photocatalytic Degradation of Organic Dye and Tetracycline Pollutants. *New J. Chem.* **2020**, *44*, 6420−6427.
(47) Moniz, S. J. A.; Shevlin, S. A.; Martin, D. J.; Guo, Z. X.; Tang, J. Visible-Light Driven Heterojunction Photocatalysts for Water Splitting-a Critical Review. *Energy Environ. Sci.* **2015**, *8*, 731−759.
(48) Golden, T. D.; Shumsky, M. G.; Zhou, Y.; VanderWerf, R. A.; Van Leeuwen, R. A.; Switzer, J. A. Electrochemical Deposition of Copper(I) Oxide Films. *Chem. Mater.* **1996**, *8*, 2499−2504.
(49) Balamurugan, B.; Mehta, B. R. Optical and Structural Properties of Nanocrystalline Copper Oxide Thin Films Prepared by Activated Reactive Evaporation. *Thin Solid Films* **2001**, *396*, 90−96.
(50) Dey, A.; Chandrabose, G.; Damptey, L. A. O.; Erakulan, E. S.; Thapa, R.; Zhuk, S.; Dalapati, G. K.; Ramakrishna, S.; Braithwaite, N. S. J.; Shirzadi, A.; Krishnamurthy, S. Cu2O/CuO Heterojunction Catalysts through Atmospheric Pressure Plasma Induced Defect Passivation. *Appl. Surf. Sci.* **2021**, *541*, No. 148571.
(51) Li, Y.; Zhang, L.; Xiang, X.; Yan, D.; Li, F. Engineering of ZnCo-Layered Double Hydroxide Nanowalls toward High-Efficiency Electrochemical Water Oxidation. *J. Mater. Chem. A* **2014**, *2*, 13250−13258.
(52) Hsu, Y. K.; Yu, C. H.; Chen, Y. C.; Lin, Y. G. Fabrication of Coral-like Cu2O Nanoelectrode for Solar Hydrogen Generation. *J. Power Sources* **2013**, *242*, 541−547.
(53) Ghosh, D.; Roy, K.; Sarkar, K.; Devi, P.; Kumar, P. Surface Plasmon-Enhanced Carbon Dot-Embellished Multifaceted Si(111) Nanoheterostructure for Photoelectrochemical Water Splitting. *ACS Appl. Mater. Interfaces* **2020**, *12*, 28792−28800.
(54) Zhou, M.; Guo, Z.; Liu, Z. FeOOH as Hole Transfer Layer to Retard the Photocorrosion of Cu2O for Enhanced Photoelctrochemical Performance. *Appl. Catal., B* **2020**, *260*, No. 118213.
(55) Niveditha, C. V.; Fatima, M. J. J.; Sindhu, S. Comprehensive Interfacial Study of Potentio-Dynamically Synthesized Copper Oxide Thin Films for Photoelectrochemical Applications. *J. Electrochem. Soc.* **2016**, *163*, H426−H433.
(56) Marathey, P.; Patel, B.; Khanna, S.; Vanpariya, A.; Ray, A. Photoelectrochemical Characteristics of Electrodeposited Cuprous Oxide with Protective over Layers for Hydrogen Evolution Reactions. *Int. J. Hydrogen Energy* **2021**, *46*, 16431−16439.
(57) Yu, R.; Chen, Q.; Li, W.; Yu, X.; Zhong, Q. Decorating Cu2O with Ni-Doped Metal Organic Frameworks as Efficient Photocathodes for Solar Water Splitting. *Int. J. Hydrogen Energy* **2023**, *48*, 17065−17073.
(58) Jeong, D.; Jo, W.; Jeong, J.; Kim, T.; Han, S.; Son, M. K.; Jung, H. Characterization of Cu2O/CuO Heterostructure Photocathode by Tailoring CuO Thickness for Photoelectrochemical Water Splitting. *RSC Adv.* **2022**, *12*, 2632−2640.
(59) Seo, Y. J.; Arunachalam, M.; Ahn, K. S.; Kang, S. H. Integrating Heteromixtured Cu2O/CuO Photocathode Interface through a Hydrogen Treatment for Photoelectrochemical Hydrogen Evolution Reaction. *Appl. Surf. Sci.* **2021**, *551*, No. 149375.
(60) John, S.; Roy, S. C. CuO/Cu2O Nanoflake/Nanowire Heterostructure Photocathode with Enhanced Surface Area for Photoelectrochemical Solar Energy Conversion. *Appl. Surf. Sci.* **2020**, *509*, No. 144703.
(61) Lin, Y. C.; Hsu, L. C.; Lin, C. Y.; Chiang, C. L.; Chou, C. M.; Wu, W. W.; Chen, S. Y.; Lin, Y. G. Sandwich-Nanostructured n-Cu2O/AuAg/p-Cu2O Photocathode with Highly Positive Onset Potential for Improved Water Reduction. *ACS Appl. Mater. Interfaces* **2019**, *11*, 38625−38632.
(62) Diao, L.; Zheng, L.; Zhang, R.; Chen, F.; Li, Y.; Wang, W.; Lu, F.; Chen, L.; Liu, H.; Dong, H.; Cheng, Y. Titanium Nitride Protected Cuprous Oxide Photocathode for Stable and Efficient Water Reduction. *ACS Appl. Energy Mater.* **2022**, *5*, 770−776.

https://doi.org/10.1021/acsomega.3c03585
ACS Omega 2023, 8, 32794−32803